A Dielectric Insular Resonator Antenna Array Fed by a Dielectric Insular Image Guide

Lukui Jin, *Student Member, IEEE,* Razak Lee, *Student Member, IEEE,* and Ian Robertson, *Fellow, IEEE*

Abstract—In this paper, a double-sided Taylor-distribution dielectric insular resonator antenna (DIRA) array fed by the dielectric insular image guide (DIIG) is presented. The analysis and design starts with the rectangular dielectric resonator (DR), then extends to the dielectric resonator antenna (DRA) and finally the DIRA. All is performed through the effective dielectric constant (EDC) method, verified by the HFSS simulation based on the finite element method (FEM). In order to enhance the gain, the DIRA array is made double-sided, *i.e.*, adding another mirror array on the other side of the DIIG. The Taylor distribution technique is employed here to suppress the sidelobe. Finally, the 10-element linear DIRA array is fabricated and measured, where a high gain of 15.8 dBi has been achieved.

Index Terms—Antenna arrays, dielectric resonator antenna, millimeter wave circuits, transmission lines, multichip modules.

I. INTRODUCTION

1939 saw the birth of a new term, "dielectric resonator (DR)", by Ritchmyer of Stanford University who found that dielectric objects in the form of toroids could function as microwave resonators and thus are potential to be developed as oscillators and filters [1]. During this time, DRs, typically cylindrical, are fabricated out of high dielectric constant materials ($\epsilon_r \geq 35$) and usually shielded to maintain the high quality factor needed for applications in oscillators, filters, *etc* [2].

By removing the shielding and with proper feeding schemes, these DRs are found to be functioning as efficient radiators. In fact, the theoretical investigations on the radiation characteristics of DRs were carried out long ago in the 1960s as a sideline and practically suppressed for the prevailing application of oscillators and filters until 1983 [3], [4]. In this year, S. Long *et al*. published a paper on the cylindrical dielectric resonator antenna (DRA) which studied and examined at length the radiation performances of DRs as antennas [5]. After that, they continued with the research on this subject to explore DRAs in other shapes: rectangle [6] and hemisphere [7]. All their serial work laid the foundation for future extensive investigations on various aspects of DRAs in various forms [8], [9].

Over the last few decades, the DRA has been drawing massive interest to prompt significant progress in microwave and mm-wave antenna technologies. What's more, a recent surge of DRA publications shown in Fig. 1 is arguably showing that the interest on this subject tends to be in an explosively-growing mode. The preference on the DRA mainly lies in the fact of its versatility, efficiency and design flexibility compared with the traditional microstrip antenna and other low-gain narrow-band antennas [10].
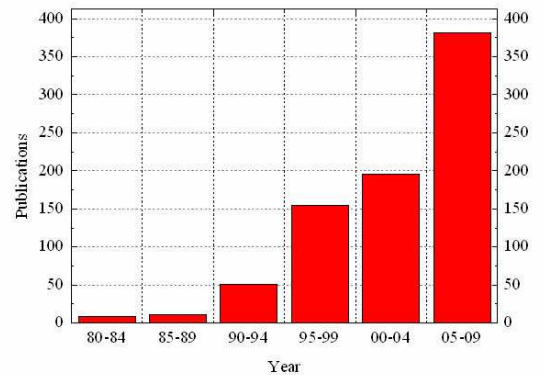
Fig. 1. The number of publications on DRAs in recent years [10].

Of all the different shapes of DRAs, the rectangular DRA offers advantages over DRAs in other shapes, such as cylindrical and spherical. One advantage is that it has two degrees of dimensional freedom. For any given resonant frequency and fixed dielectric constant, two of the three dimensions of the rectangular DRA can be chosen independently (one for the cylindrical DRA and none for the hemispherical DRA), which provides more flexibility in terms of aspect ratios and thus bandwidth control [9], [11]. The other is that mode degeneracy, which can enhance the cross-pol levels of an antenna and should be strongly avoided, can be removed in rectangular DRAs; while it always exists in a spherical DRA and in the hybrid modes of a cylindrical DRA [3], [11], [12].

As for the feeding scheme of the DRA, the aperture, coaxial probe, coplanar waveguide, microstrip line or dielectric image guide (DIG) have all been used [2], [8], [9]. Among the various methods, the DIG coupling to the DRA offers advantages over the microstrip line in that it does not suffer from severe conductor loss, especially in the mm-wave band. What's more, this conductor loss could be further reduced by introducing a low-permittivity insular layer between the dielectric guide and the ground plane, namely employing dielectric insular image guide (DIIG) [13]. With the DIIG as the feeding line, the DRA also has an insular layer underneath it, which is thus named as "DIRA (dielectric insular resonator antenna)". Similar to the microstrip line coupling, DIRAs can be fed either from sideways or underneath through DIG. This feeding scheme is promising and has found its way in many applications, especially in the series-fed linear DRA array [2], [8], [14], [15].

This paper proposes a linear rectangular DIRA array

sideways-fed by a DIIG on the same level. In order to enhance the gain of the DIRA array and increase the coupling between the DIIG and DIRA, the radiating elements of the DIRA array are placed on both sides of the DIIG. The theoretical analysis starts with the rectangular DR, then extends to the DRA and finally the DIRA in Sections II and III. In Section IV, the coupling mechanism between the DIIG and DIRA is studied, which leads to the design and measurement of a double-sided Taylor-distributed DIRA array.

II. RESONANT MODES OF RECTANGULAR DR

The resonant mode is generated for a microwave resonator, including the DR, when the stored electric energy is equal to the magnetic energy. Generally, there will be an infinite number of resonant modes and each of them corresponds to a particular resonant frequency. Only the lowest order or a couple of low-order modes will be of interest in the scientific research and practical applications. As for the DR, there are no metallic surfaces to completely confine electromagnetic fields inside, which gives rise to the leakage or radiation in a specific field pattern at a specific mode. That's basically how a DRA is formed [8].

A rectangular DR can be viewed as a truncated DG engulfed in the air, as shown in Fig. 2(a), (b). So the modes in a rectangular DR is similar to that in a DG, except that the wave will be standing (suppose there is a field variation) along the z direction instead of travelling. Theoretical methods to analyse the propagation characteristics of the DG/DIG, such as Marcatili's method [16] and the EDC method [17], can be easily transferred to that of the DR. In order for the DR to be used as a DRA in the microwave and mm-wave band and also for the facility of feeding, the DR is practically placed on top of a pure or insulated metal together with the feeding DIG/DIIG, as shown in Fig. 2(c), (d) [9], [18].

On one hand, the rectangular DR enjoys more design flexibility compared with the spherical or cylindrical DR, which comes from the three independent dimensions; on the other hand, this edge-rich shape brings in more discontinuities and hence, more complexity of its field distribution. In fact, all 6 components of electric and magnetic fields exist in the rectangular DG and hence, the rectangular DR [19]. By contrast, only TE, TM or the combination of these two modes reside in the spherical and cylindrical DR [3], [12]. By neglecting the weakest electric or magnetic components, however, the modes of the rectangular DR can be grouped into TE-like and TM-like ones, as demonstrated in [16] for the DG.

Based on the nomenclature used for the rectangular DG [16], the propagating modes can be classified into TM_{mn}^y and TE_{mn}^y modes. For the TM_{mn}^y mode, E_y and H_x are the principal transverse field components, whereas E_x and H_y are taken as the strongest transverse components when the TE_{mn}^y mode is separated. Following this nomenclature, the resonant modes of a rectangular DR as a truncated section of a DG is thus specified as TM_{mnl}^y and TE_{mnl}^y modes. The mode indices, m, n, and l, refer to the number of field extremas or half cycle variations of electric and magnetic components

(a) An infinite DG   (b) DR (truncated DG)

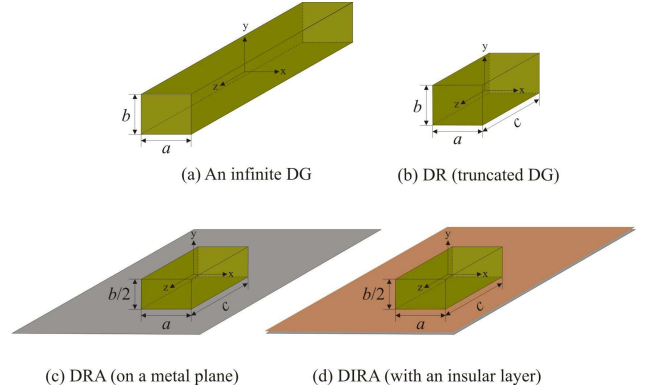(c) DRA (on a metal plane)   (d) DIRA (with an insular layer)

Fig. 2. The 3D geometry of a DG, DR, DRA and DIRA.

inside the DR along x, y, and z directions, respectively. At resonant frequencies, the fields tend to be standing inside the DR (except when m, n, or l equals 0), whereas decaying exponentially with distance outside it [18].

For the record, it's not just the TM_{mnl}^y and TE_{mnl}^y modes that can reside inside a rectangular DR. R. Mongia, $et.al.$, point out that TE and TM modes to other directions, $i.e.$, x, z, are also possible if the three dimensions of the resonator are not very different from each other [11], [20].

III. RESONANT MODEL OF RECTANGULAR DRA AND DIRA

Since a rectangular DR can be viewed as a truncated DG, as shown in Fig. 2, the rectangular DG model is generally used to describe the wave behaviours in and around the DR. As for the characterization of DGs, there are two popular approximate methods, Marcatili's method and the EDC method, as demonstrated in [16], [17]..

If the DG is truncated in the z direction to form a DR and hence, a DRA, as shown in Fig. 2, there could also be a standing-wave pattern triggered inside the DR and an exponentially-decaying wave outside it along that direction, as is the case along the x and y directions.

Following the analysis on the DIG in [17] through the EDC method, assumptions can be made that the propagation constants along the x and y directions, k_{x1} and k_{y1}, stay unchanged, while a similar characteristic equation can then be set up along the z direction.

A. DRA

The rectangular DRA to be studied is shown in Fig. 2(c). For the TM_{mnl}^y mode, the characteristic equations in the x and y directions have already been given in [17] as:

$$k_{x1}a = -2\arctan\left(\frac{k_{x1}}{k_{x0}}\right) + m\pi$$

$$k_{y1}b = -2\arctan\left(\frac{k_{y1}}{\epsilon_r k_{y0}}\right) + n\pi \tag{1}$$

where

$$k_{x1} = \sqrt{\epsilon_{re}k_0^2 - \beta_{v1}^2}, \quad k_{x0} = \sqrt{(\epsilon_{re} - 1)k_0^2 - k_{x1}^2}$$

$$k_{y1} = \sqrt{\epsilon_r k_0^2 - \beta_h^2}, \quad k_{y0} = \sqrt{(\epsilon_r - 1)k_0^2 - k_{y1}^2}$$

$$\epsilon_{re} = \epsilon_r - \left(\frac{k_{y1}}{k_0}\right)^2 \tag{2}$$

$$m = 2m' - 1, \quad m' = 1, 2, 3, \cdots \quad \text{even mode}$$
$$m = 2m', \quad m' = 1, 2, 3, \cdots \quad \text{odd mode}$$
$$n = 2n' - 1, \quad n' = 1, 2, 3, \cdots$$

Now that in the z direction can be derived through the EDC method as:

$$k_{z1}c = -2\arctan\left(\frac{k_{z1}}{k_{z0}}\right) + l\pi \tag{3}$$

where

$$k_{z1} = \sqrt{\epsilon_{re}k_0^2 - \beta_{v2}^2}, \quad k_{z0} = \sqrt{(\epsilon_{re} - 1)k_0^2 - k_{z1}^2}$$

$$l = 2l' - 1, \quad l' = 1, 2, 3, \cdots \quad \text{even mode} \tag{4}$$
$$l = 2l', \quad l' = 1, 2, 3, \cdots \quad \text{odd mode}$$

Note that k_{x1}, k_{y1}, and k_{z1} should also satisfy the separation equation

$$\epsilon_r k_0^2 = k_{x1}^2 + k_{y1}^2 + k_{z1}^2 \tag{5}$$

Solve the equation array, (1), (3) and (5) for k_0 and hence, the resonant frequency

$$f_0 = \frac{k_0 c_0}{2\pi} \tag{6}$$

where c_0 is the speed of light in the free space.

For the TE_{mnl}^y mode, the characteristic equations in the x, y, and z directions can be derived through the EDC method as:

$$k_{x1}a = -2\arctan\left(\frac{k_{x1}}{\epsilon_{re}k_{x0}}\right) + m\pi$$

$$k_{y1}b = -2\arctan\left(\frac{k_{y1}}{k_{y0}}\right) + n\pi \tag{7}$$

$$k_{z1}c = -2\arctan\left(\frac{k_{z1}}{\epsilon_{re}k_{z0}}\right) + l\pi$$

where

$$m = 2m', \quad m' = 1, 2, 3, \cdots \quad \text{even mode}$$
$$m = 2m' - 1, \quad m' = 1, 2, 3, \cdots \quad \text{odd mode}$$
$$n = 2n', \quad n' = 1, 2, 3, \cdots$$
$$l = 2l', \quad l' = 1, 2, 3, \cdots \quad \text{even mode}$$
$$l = 2l' - 1, \quad l' = 1, 2, 3, \cdots \quad \text{odd mode}$$

and k_{xi}, k_{yi}, and k_{zi}, $i = 0, 1$, are defined in (2) and (4).

After that, the resonant frequency of the TE_{mnl}^y mode follows the same derivation procedure as the TM_{mnl}^y mode.

As for the TE and TM modes to the x and z directions, they can be derived and expressed in a similar way and therefore, wll not be repeated here.

One thing to be noted is that the subindex which corresponds to the superindex can be 0, e.g., for the TE_{mnl}^x mode, m can start from 0, whereas for the TE_{mnl}^z mode, it's z that
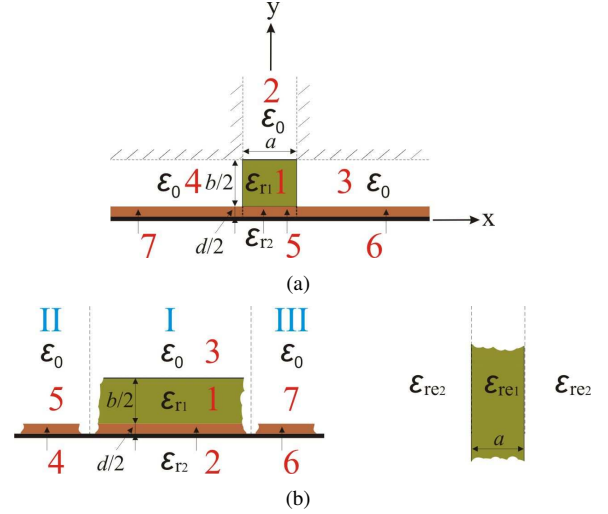

Fig. 3. The cross-sectional view of: (a) the DIRA, (b) equivalent horizontal and vertical slab guides for the EDC method.

can be 0, unless restrained by the metallic ground plane. This is an obvious difference between the DRA and DIG, which means that the fields can now be uniformly distributed in one specific direction in the DRA.

B. DIRA

The rectangular DIRA to be studied is shown in Fig. 2(d) and its cross-sectional view for the EDC method is shown in Fig. 3. For the TM_{mnl}^y mode, the characteristic equations in the x, y, and z directions are derived through the EDC method as:

$$1 + \frac{k_{x0}^2 - k_{x1}^2}{k_{x0}k_{x1}}\tan(k_{x1}a/2) - \tan^2(k_{x1}a/2) = 0$$

$$1 + \frac{k_{y2}}{\epsilon_{r2}k_{y3}}\tanh(k_{y2}d/2) - \frac{k_{y1}}{\epsilon_{r1}k_{y3}}\tan(k_{y1}b/2)$$

$$+ \frac{\epsilon_{r1}k_{y2}}{\epsilon_{r2}k_{y1}}\tanh(k_{y2}d/2)\tan(k_{y1}b/2) = 0, \quad \text{Region I} \tag{8}$$

$$1 - \frac{k_{y4}}{\epsilon_{r2}k_{y5}}\tan(k_{y4}d/2) = 0, \quad \text{Regions II \& III}$$

$$1 + \frac{k_{z0}^2 - k_{z1}^2}{k_{z0}k_{z1}}\tan(k_{z1}c/2) - \tan^2(k_{z1}c/2) = 0$$

where

$$k_{x1} = \sqrt{\epsilon_{re1}k_0^2 - \beta_{v1}^2}, \quad k_{x0} = \sqrt{(\epsilon_{re1} - \epsilon_{re2})k_0^2 - k_{x1}^2}$$

$$k_{y1} = \sqrt{\epsilon_{r1}k_0^2 - \beta_{h1}^2}$$

$$k_{y2} = \sqrt{(\epsilon_{r1} - \epsilon_{r2})k_0^2 - k_{y1}^2}, \quad k_{y3} = \sqrt{(\epsilon_{r1} - 1)k_0^2 - k_{y1}^2}$$

$$k_{y4} = \sqrt{\epsilon_{r2}k_0^2 - \beta_{h2}^2}, \quad k_{y5} = \sqrt{(\epsilon_{r2} - 1)k_0^2 - k_{y4}^2}$$

$$k_{z1} = \sqrt{\epsilon_{re1}k_0^2 - \beta_{v2}^2}, \quad k_{z0} = \sqrt{(\epsilon_{re1} - \epsilon_{re2})k_0^2 - k_{z1}^2}$$

$$\epsilon_{re1} = \epsilon_{r1} - \left(\frac{k_{y1}}{k_0}\right)^2, \quad \epsilon_{re2} = \epsilon_{r2} - \left(\frac{k_{y4}}{k_0}\right)^2 \tag{9}$$

After that, the resonant frequency follows the same derivation procedure as the TM_{mnl}^y mode of the DRA.

For the TE^y_{mnl} mode, the characteristic equations in the x, y, and z directions are derived through the EDC method and given in a similar mannar as the TM^y_{mnl} mode:

$$1 + \frac{(\epsilon_{re1}k_{x0})^2 - (\epsilon_{re2}k_{x1})^2}{\epsilon_{re1}\epsilon_{re2}k_{x0}k_{x1}}\tan(k_{x1}a/2)$$
$$- \tan^2(k_{x1}a/2) = 0$$

$$1 + \frac{k_{y3}}{k_{y2}}\tanh(k_{y2}d/2) + \frac{k_{y3}}{k_{y1}}\tan(k_{y1}b/2)$$
$$- \frac{k_{y1}}{k_{y2}}\tanh(k_{y2}d/2)\tan(k_{y1}b/2) = 0, \quad \text{Region I} \quad (10)$$

$$1 - \frac{k_{y4}}{k_{y5}}\tan(k_{y4}d/2) = 0, \quad \text{Regions II \& III}$$

$$1 + \frac{(\epsilon_{re1}k_{z0})^2 - (\epsilon_{re2}k_{z1})^2}{\epsilon_{re1}\epsilon_{re2}k_{z0}k_{z1}}\tan(k_{z1}a/2)$$
$$- \tan^2(k_{z1}a/2) = 0$$

where k_{xi}, k_{yi}, and k_{zi}, $i = 0$, 1, are defined in (9).

After that, the resonant frequency follows the same derivation procedure as the TM^y_{mnl} mode of the DRA.

IV. Design of a DIRA array Fed by the DIIG

In this section, a linear DIRA array is designed, simulated, and measured. In order to enhance the gain, the DIRA array is made double-sided, *i.e.*, adding another mirror array on the other side of the DIIG. The Taylor distribution is employed here to suppress the sidelobe.

A. Resonant Mode and Length

A low-loss DIIG designed through the EDC method will be used here as the feeding line and hence, transforms the DRA into DIRA. The fundamental mode propagating in the DIIG is TM^y_{11} with a main H_x component, which couples into the nearby DIRA with the same corss-section and triggers the resonant modes with H_x as one of their main field components: TM^y_{11l}, TM^z_{11l}, and TE^x_{11l} modes. It can be further revealed that the remaining field components are E_y, H_z for the TM^y_{11l} modes, H_y, E_z for the TM^z modes, and E_y, E_z for the TE^x modes. These modes should be carefully separated in the DIRA array design in order to avoid the radiation interference.

The Dupont^{TM} GreenTape^{TM} 9K7 LTCC system is used as the main dielectric material of the DIIG, which has a relative dielectric constant, ϵ_{r1} of 7.1 at 10 GHz. Its loss tangent is also characterised at 10 GHz to be $\tan\delta = 0.001$. The material used as the metallic ground plane here is copper plated on a RT/duroid 5880 board, which has a conductivity of $\sigma = 5.8e7$ S/m, a relative dielectric constant, ϵ_{r2} of 2.2 and a loss tangent of 0.001 at 10 GHz. The designed DIIG works in the Ka band with a cross-section of $a = 1.32$ mm, $b/2 = 1.54$ mm, $p = 0.16$. The DIRA has the same cross-section to achieve the maximum coupling [21], which leaves the length, c, as a flexible variable. It is then used to tune the DIRA to resonate at 35 GHz.

Table I lists a set of some possible modes resonating at 35 GHz. Since the guided wavelength at 35 GHz for the TM^y_{11} mode is calculated to be 6.16 mm, the 113 and higher-order

TABLE I
THE LENGTH, c, OF THE DIRA FOR SOME POSSIBLE MODES RESONATING AT 35 GHz.

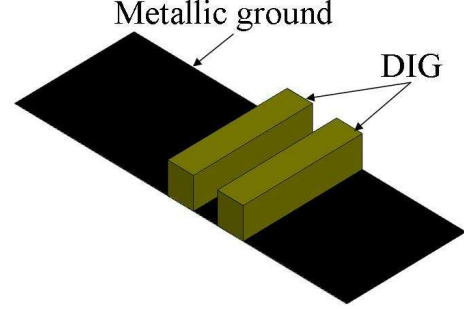| Mode order	111			112			113		
Mode type	TM^y	TM^z	TE^x	TM^y	TM^z	TE^x	TM^y	TM^z	TE^x
c (mm)	0.9	2	1.7	3.5	4.3	4.3	5.9	6.6	6.8

Fig. 4. Symmetric or asymmetric modes for the coupling between two DIGs [17].

modes need double-wavelength feeding line and thus are not suitable for compact antenna designs.

As for the 111 and 112 modes, TM^z and TE^x stay too close to be differentiated, which leaves the TM^y modes as the only option. In the following subsection, they will be further reduced into one specific mode as the best candidate based on the coupling between the feeding line and radiating elements.

B. Coupling

1) Between the DIG and DRA: Firstly, consider the coupling between two DIGs with the same cross-section, as shown in Fig. 4. The reason for choosing the same cross-section is to achieve maximum coupling, which has been concluded in [21]. Now the structure under investigation is symmetrical with respect to the $x = 0$ plane and hence, the fields propagating along the DIGs can be classified into symmetrical (even) and asymmetrical (odd) groups depending on whether it's a electric or magnetic wall at the $x = 0$ plane. Further, the symmetrical and asymmetrical modes will inevitably generate different phase velocities, which is the root of coupling [16], [17].

We now apply the EDC method to carry out the coupling analysis between two DIGs, where only the TM^y_{mn} mode will be considered, as the fundamental operating mode in the DIG is TM^y_{11}.

The characteristic equations and the effective dielectric constant, ϵ_{re}, have already been given by (1) and (2). Now the wavenumber in the x direction, k_{x1}, needs to be rewritten, in the light of the new configuration in that direction, as [17]:

$$k_{x1}a = -\arctan\left(\frac{k_{x1}}{k_{x0}}\right) - \arctan\left(\frac{Dk_{x1}}{k_{x0}}\right) + m\pi \quad (11)$$

where

$$m = 1,\ 2,\ 3,\ \cdots$$
$$D = \coth(k_{x0}g/2), \quad \text{even mode}$$
$$= \tanh(k_{x0}g/2), \quad \text{odd mode}$$

So k_{x1} now comprises two values, k_{xe} for the even mode and k_{xo} for the odd mode. Hence, the phase constant, β (equals k_z in a low-loss situation), can be derived in two forms:

$$\begin{aligned}
\beta_e = \sqrt{\epsilon_{re}k_0^2 - k_{xe}^2}, \quad &\text{even mode} \\
\beta_o = \sqrt{\epsilon_{re}k_0^2 - k_{xo}^2}, \quad &\text{odd mode}
\end{aligned} \tag{12}$$

In order to be connected with the propagation in a single DIG, β_e and β_o can be rewritten as [16]:

$$\left.\begin{aligned}\beta_e \\ \beta_o\end{aligned}\right\} = \beta\left[1 \pm 2\frac{k_x^2}{\beta^2}\frac{1}{k_{x0}a}\frac{\exp(-k_{x0}g)}{1 + k_x^2/k_{x0}^2}\right],$$

where β and k_x are the phase constant and x-direction wavenumber of the single DIG, respectively.

Then we define the coupling coefficient, K, between the two DIGs as:

$$\begin{aligned}
-jK &= \frac{\beta_e - \beta_o}{2} \\
&= 2\frac{k_x^2}{\beta^2}\frac{1}{k_{x0}a}\frac{\exp(-k_{x0}g)}{1 + k_x^2/k_{x0}^2}
\end{aligned} \tag{13}$$

and the length, L, necessary for complete power transfer from one DIG to the other is then derived as:

$$L = \frac{\pi}{2|K|}. \tag{14}$$

Now the second DIG is truncated to form a DRA and the coupling mechanism follows the same rule as that of two DIGs.

As predicted, the coupling is enhanced exponentially by decreasing either the gap, g, or the real attenuation constant, k_{x0}, whereas by changing the length, c, of the DRA, the coupling fluctuates square-sinusoidally as [15], [22]

$$K_p = \sin^2\left(\frac{\pi c}{2L}\right) \tag{15}$$

where K_p is the power coupling coefficient which stands for the ratio of coupled power to the DRA from the feeding DIG.

In order to verify those conclusions, a 3D simulator, HFSS, based on the FEM method is used to calculate this coupling problem for the fundamental TM_{11}^y mode, as shown in Fig. 4. The configurational parameters are that $a = b = 1$ mm and $\epsilon_r = 7.1$. Results are shown in Fig. 5.

In Fig. 5(a), g is fixed to be 0.5 mm and the corresponding L for complete power transfer (where $K_p = 1$) is calculated through the EDC method to be 10.4 mm. Then, substitute it for L in (15) to obtain the theoretical result. As expected, the curve takes the shape similar to a square sinusoid. The result from HFSS has also been provided as a comparison. It can be seen that the peak and valley positions agree well, while the peak value from the HFSS simulation can only go up to 0.7 compared to theoretical 1. The reason for this is probably because unaccounted loss in theoretical calculation is revealed in the more practical HFSS simulation.

In Fig. 5(b), c is fixed to be 3 mm. By changing g, L is changed and K_p is affected in the end. Results from HFSS and the EDC method agree well and they all descend quickly as the gap, g increases, which is predicted by the preceding conclusion.
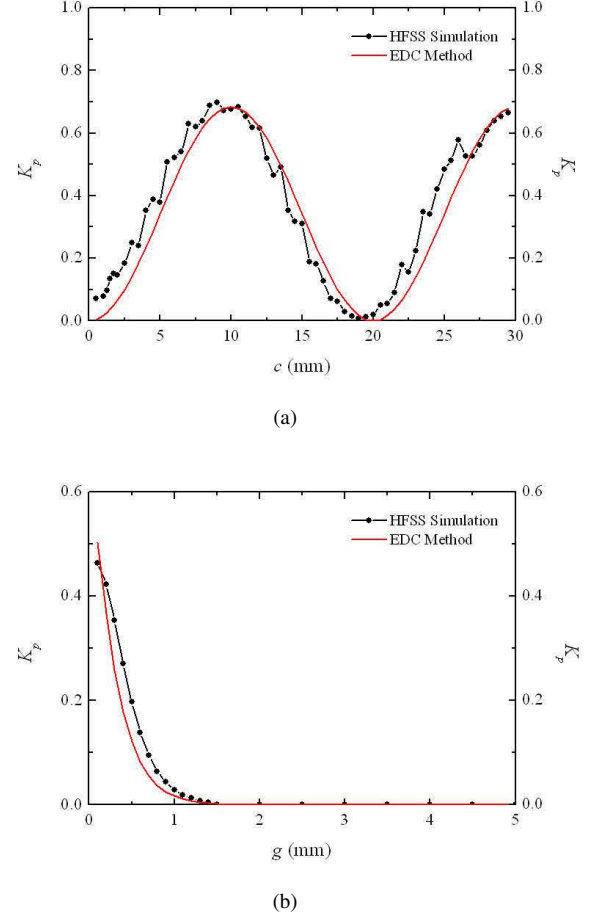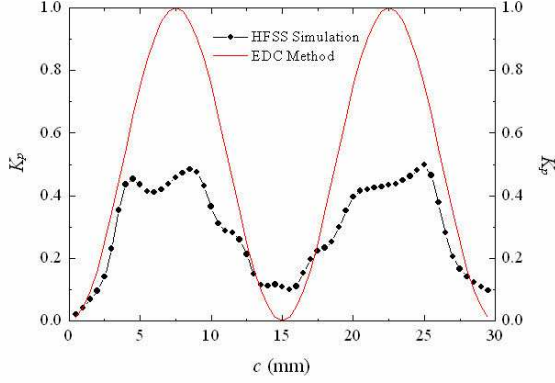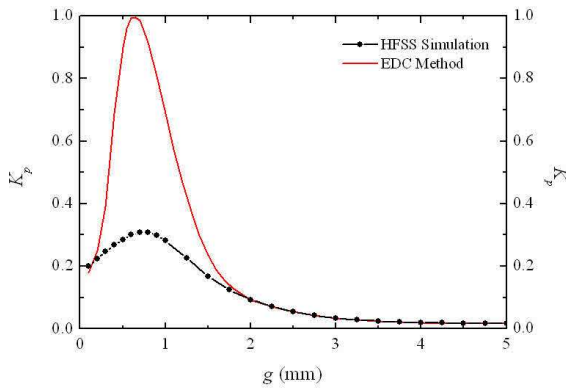

(a)

(b)

Fig. 5. The power coupling coefficient, K_p, of the TM_{11}^y mode between the DIG and DRA ($a = b = 1$ mm, $\epsilon_r = 7.1$): (a) $g = 0.5$ mm and c varies, (b) $c = 3$ mm and g varies.

2) Between the DIIG and DIRA: Through (13) and (14), L is obtained for the DIRA as 7.5 mm. Then, K_p with various c's and g's is analysed and shown in Fig. 6. As can be seen, results from HFSS and the EDC method agree well in terms of the shape and positions of peaks and valleys. The coupled power from the EDC method is obviously lower possibly for the same reason in the DRA case. One thing to be noted, however, is that K_p doesn't drop quickly to 0 in Fig. 6(b). In fact, a residual coupled power still exists even when the DIIG and DIRA are 5 mm apart. The reason is that the insular layer binds the DIIG and DIRA together and works as a chanel where power couples. This will inevitably slows down the fade-away speed of power coupling.

As presented in Subsection IV-A, the resonant frequency of 35 GHz under the DIIG-feeding scheme has only left two options for the resonant modes of the DIRA: TM_{111}^y and TM_{112}^y. In order to achieve high level of coupling, the TM_{112}^y mode is chosen as its resonant length, c, is closer to L compared with the TM_{111}^y mode. It's also worth mentioning that still K_p is very low for the TM_{112}^y mode, even at its peak value (about 0.3). To obtain higher antenna gain and more flexibility in antenna design, higher power coupling is needed.

(a)

(b)

Fig. 6. The power coupling coefficient, K_p, of the TM_{11}^y mode between the DIIG and DIRA ($a = b = 1$ mm, $p = 0.2$ $\epsilon_r = 7.1$): (a) $g = 0.5$ mm and c varies, (b) $c = 3.5$ mm and g varies.
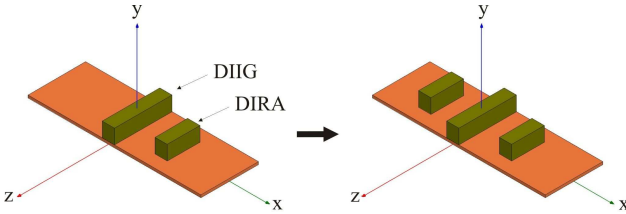

Fig. 7. The transformation from single-sided to double-sided DIRA.

C. Double-sided Taylor-distribution

In order to achieve higher power coupling, the original DIRA fed by the DIIG in [14], [15] is improved by adding a mirror array of DIRA blocks on the other side. As a result, the DIRA array now becomes double-sided, as shown in Fig. 7. The two DIRA block arrays are coupled to the DIIG by an H_x component and are thus resonant in the same TM_{112}^y mode. With more receptors to couple, the power coupling coefficient, K_p is now certainly higher.

This is verified through the HFSS simulation on the double-sided DIRA shown in Fig. 7, where the DIIG is one guided-wavelength long (6.16 mm). Results are shown in Fig. 8. It can be seen that the peak K_p has increased to nearly 0.45,
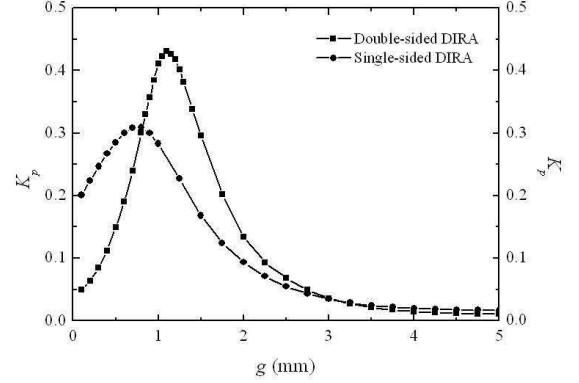

Fig. 8. The comparison of the coupling coefficient, K_p, between the single-sided and double-sided DIRA.

whereas the peak position has shifted upwards from $c = 0.8$ mm to 1.1 mm.

For a practical antenna array, it is always desirable to have a main beam as narrow as possible, a gain as high as possible and a side lobe as low as possible, which, in many cases, is hard to realise. Since several decades ago, two methods have been developed and widely used to do the compromise: Dolph-Tchebysheff distribution [23] and Taylor distribution [24], [25]. For the Dolph-Tchebysheff distribution, the width of the main beam is the narrowest that a symmetric array can get at the prescribed side-lobe level, whereas the drawback of this method is that all its side lobes are at the same level, even extending to infinity. The Taylor distribution, however, has side lobes which are gradually vanishing, by sacrificing some main-beam width.

In this design, the Taylor distribution is chosen to minimise the side-lobe level.

To start the Taylor distribution, the number of DIRA elements in the array needs to be determined based on the prescribed gain. Here at least a 15 dB gain is needed, which requires 10 elements or more. Next is to prescribe the side-lobe level at 20 dB or 25 dB.

Then, the original Taylor distribution of 10 array elements for 20-dB and 25-dB side-lobe level are calculated and shown in Table II. Note that the power distribution is recalculated here. The reason is because when the energy travels through an element, a portion is absorbed and thus the energy injected into the next element is the residual from the total. Hence, the power ratio is calculated based on the residual. Results are also shown in Table II. Note that all the power feeding is realised through the coupling between the DIIG and DIRA, i.e., K_p.

As can be observed in Table II, K_p of the last element in the recalculated Taylor distribution is 1. This is not hard to achieve, as the last element will be open ended and radiate most of the power easily. For the other elements, however, it has to stay below the peak K_p of the double-sided DIRA in Fig. 8. This will rule out the application of the 25-dB distribution, as Elements 7, 8, and 9 are on top of the threshhanold.

TABLE II
THE TAYLOR DISTRIBUTION OF 10 ARRAY ELEMENTS IN TERMS OF
POWER.

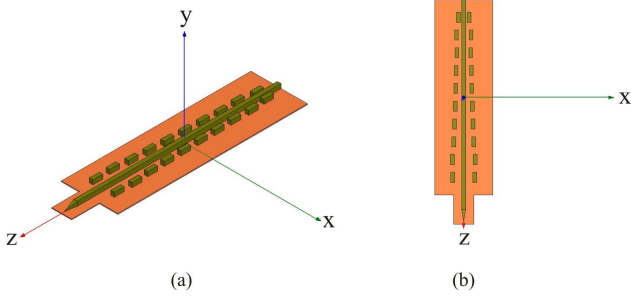| Element	20 dB (original)	20 dB (recalculated)	g (mm)	25 dB (original)	25 dB (recalculated)
1	0.070	0.070	2.47	0.030	0.030
2	0.051	0.054	2.67	0.046	0.047
3	0.096	0.110	2.15	0.096	0.104
4	0.129	0.165	1.89	0.147	0.177
5	0.154	0.235	1.66	0.182	0.267
6	0.154	0.308	1.47	0.182	0.364
7	0.129	0.372	1.32	0.147	0.461
8	0.096	0.444	1.10	0.096	0.558
9	0.051	0.418	1.20	0.040	0.605
10	0.070	1.000	0.50	0.030	1.000

Fig. 9. The geometric configurations of the double-sided Taylor-distributed DIRA array: (a) 3D view, (b) top view.

After finalising the side-lobe level, the next step is to find the corresponding gap, g, which enables that amount of power coupling, by referring to Fig. 8. It's worth noting that one K_p might prompt two $g's$. For the convenience of fabrication and also to minimise the influence of fabrication errors, all $g's$ are to be chosen from the gentle slope rather than the sharp one.

The final set of $g's$ are also shown in Table II, where g for Element 10 is flexible in a wide range as the

D. Simulation and Comparison

The DIRA array needs transitions to be connected with WR28 for practical measurement and application, as shown in Fig. 9. As can be seen, only one tapered transition is added at the input end of the DIRA array in order to be fed from a standard WR28, as the energy almost dies out at the other end. Note that the transition is tapered at both horizontal and vertical planes to ensure a smooth feeding.

After optimised by the HFSS simulation, the performance of this double-sided Taylor-distributed DIRA array is given by Fig. 10.

In Fig. 10(a), the gain of both double-sided and single-sided DIRA array are shown from 30 to 40 GHz. As can be found, the peak gains center around 35 GHz and those of the double-sided array are all higher than the single-sided one. Average gain increase is from 1.5 to 2.5 dB. As for the impedance bandwidth represented by S_{11}, it is very wide, nearly throughout the whole 10-GHz band.

The radiation pattern is shown in Fig. 10(b) as the solid lines, where 34, 35, and 36 GHz are all included. The side-lobe suppression has been observed as the best side-lobe level is 17.5 dB at 35 GHz. Possible reason for the 2.5 dB
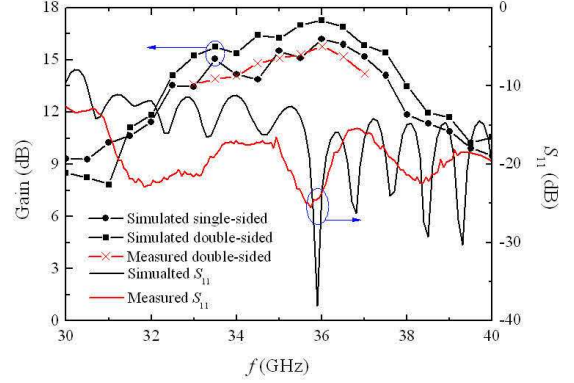
(a)
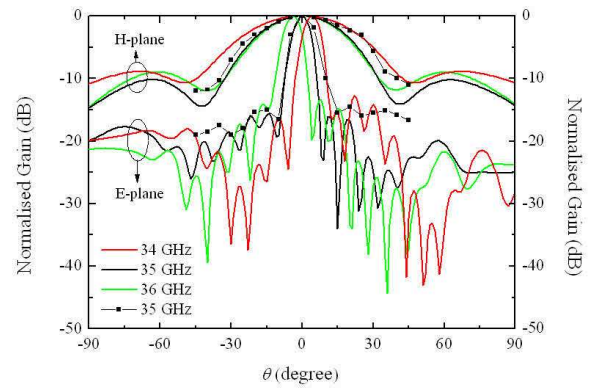
(b)

Fig. 10. The performance of the double-sided Taylor-distributed DIRA array: (a) gain and S_{11}, (b) radiation pattern (solid line for the simulation, squares for the measurement).
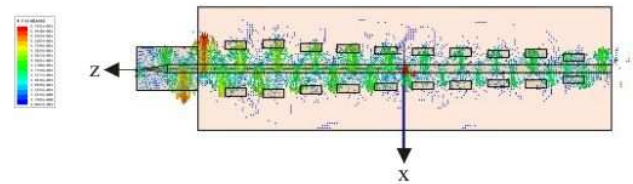

Fig. 11. The magnetic field pattern of the double-sided Taylor-distributed DIRA array.

degradation is that the cross coupling between nearby elements are not accounted for in the design process (optimisation of the cross coupling is too complicated for a 10-element array and thus will not be carried out here) and the transition added afterwards might disturb the field pattern of radiation. As there is no side-lobe suppression technique applied in the H-plane, a 10-dB sidelobe can be found. An interesting characteristic for the E-plane radiation pattern is that as frequency varies, the peak-gain position changes accordingly. This, in fact, occurs to all antenna arrays fed at one end, which in some literatures are called Long-Line Effect, [26].

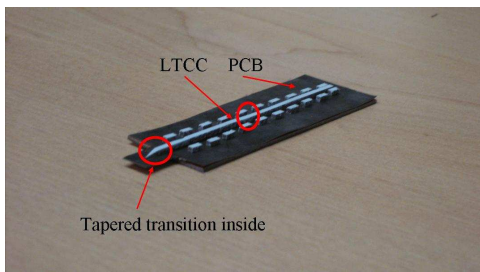Finally, the magnetic field pattern responsible for the power

Fig. 12. The fabricated 10-element double-sided DIRA array.

coupling is obtained through the HFSS simulation and presented in Fig. 11. As observed in this figure, the magnetic field is mainly in the x direction, $i.e.$, H_x. It is strong at the input of the array and gradually dies out as the field travels through the array. In the end, the last bit of power radiates at the open end. Since the array elements are all one-wavelength away, they are in phase or the H_x components are in the same direction, as shown in Fig. 11.

E. Measurement

A standard LTCC technique is used here to fabricate the 10-element double-sided DIRA array, as shown in Fig. 12.

The measured S_{11} and peak gain of the DIRA array is shown in Fig. 10(a) as the red lines. As can be observed, the measured S_{11} tends to have multiple resonances which is in line with that from the HFSS simulation. The measured gain of the double-sided array also centres around 36 GHz, although the peak gain is 1.5 dB lowered to 15.8 dBi compared with 17.3 dBi from the HFSS simulation.

The measured radiation pattern at 35 GHz is at a 5° increment up to 45° and is shown in Fig. 10(b) as the solid lines with squares. It can be seen that the main beams in both E- and H-planes get wider toward the transition end and hence, the sidelobe suppression on that side degrades by about 1.5 dB to 16 dB. Also, the measured radiation pattern cannot fully demonstrate the peaks and valleys among the sidelobes. Possible reasons for the disagreement and degradation may come from the unaccounted shrinkage of the LTCC and the bond between the LTCC and PCB board might not be completely intact.

V. CONCLUSION

Through the EDC method, this paper studies the DRA and DIRA in depth in terms of resonant modes, resonant frequencies, and field patterns. After that, a 10-element double-sided Taylor-distributed DIRA array is designed, simulated, and measured. Results agree well, which verifies the design of this antenna array.

ACKNOWLEDGMENT

REFERENCES

[1] R. D. Richtmyer, "Dielectric resonators," *Journal of Applied Physics*, vol. 10, no. 6, pp. 391 –398, Jun. 1939.
[2] A. Petosa, *Dielectric Resonator Antenna Handbook*. Artech House Publishers, 2007.
[3] M. Gastine, L. Courtois, and J. Dormann, "Electromagnetic resonances of free dielectric spheres," *Microwave Theory and Techniques, IEEE Transactions on*, vol. 15, no. 12, pp. 694 –700, Dec. 1967.
[4] O. Sager and F. Tisi, "On eigenmodes and forced resonance-modes of dielectric spheres," *Proceedings of the IEEE*, vol. 56, no. 9, pp. 1593 – 1594, Sept. 1968.
[5] S. Long, M. McAllister, and L. Shen, "The resonant cylindrical dielectric cavity antenna," *Antennas and Propagation, IEEE Transactions on*, vol. 31, no. 3, pp. 406 – 412, May 1983.
[6] M. McAllister, S. Long, and G. Conway, "Rectangular dielectric resonator antenna," *Electronics Letters*, vol. 19, no. 6, pp. 218 –219, Mar. 1983.
[7] M. McAllister and S. Long, "Resonant hemispherical dielectric antenna," *Electronics Letters*, vol. 20, no. 16, pp. 657 –659, Aug. 1984.
[8] J. L. Volakis, Ed., *Antenna Engineering Handbook*, 4th ed. McGraw-Hill Professional, 2009.
[9] K. M. Luk and K. W. Leung, Eds., *Dielectric Resonator Antennas*. Research Studies Press, 2002.
[10] A. Petosa and A. Ittipiboon, "Dielectric resonator antennas: A historical review and the current state of the art," *Antennas and Propagation Magazine, IEEE*, vol. 52, no. 5, pp. 91 –116, Oct. 2010.
[11] R. Kumar Mongia and A. Ittipiboon, "Theoretical and experimental investigations on rectangular dielectric resonator antennas," *Antennas and Propagation, IEEE Transactions on*, vol. 45, no. 9, pp. 1348 –1356, Sept. 1997.
[12] D. Kajfez and P. Guillon, Eds., *Dielectric resonators*. Norwood, MA: Artech, 1986.
[13] R. Knox, "Dielectric waveguide microwave integrated circuits - an overview," *Microwave Theory and Techniques, IEEE Transactions on*, vol. 24, no. 11, pp. 806 – 814, Nov. 1976.
[14] M. Birand and R. Gelsthorpe, "Experimental millimetric array using dielectric radiators fed by means of dielectric waveguide," *Electronics Letters*, vol. 17, no. 18, pp. 633–635, 1981.
[15] A. Al-Zoubi, A. Kishk, and A. Glisson, "A linear rectangular dielectric resonator antenna array fed by dielectric image guide with low cross polarization," *Antennas and Propagation, IEEE Transactions on*, vol. 58, no. 3, pp. 697–705, 2010.
[16] E. A. J. Marcatili, "Dielectric rectangular waveguide and directional coupler for integrated optics," *Bell System Technical Journal*, vol. 48, pp. 2071 –2102, Sept. 1969.
[17] R. M. Knox and P. P. Toulios, "Integrated circuits for the millimeter through optical frequency range," in *Proceedings of the Symposium on Submillimeter Waves*, Mar. 1970.
[18] S. K. Koul, Ed., *Millimeter Wave and Optical Dielectric Integrated Guides and Circuits*, 1st ed. Wiley-Interscience: New York, 1997.
[19] A. Oliner, S.-T. Peng, T.-I. Hsu, and A. Sanchez, "Guidance and leakage properties of a class of open dielectric waveguides: Part ii–new physical effects," *Microwave Theory and Techniques, IEEE Transactions on*, vol. 29, no. 9, pp. 855 – 869, Sept. 1981.
[20] R. Mongia, "Theoretical and experimental resonant frequencies of rectangular dielectric resonators," *Microwaves, Antennas and Propagation, IEE Proceedings H*, vol. 139, no. 1, pp. 98 –104, Feb. 1992.
[21] M. Wyville, A. Petosa, and J. Wight, "Dig feed for dra arrays," in *Antennas and Propagation Society International Symposium, 2005 IEEE*, vol. 2A, 2005, pp. 176–179 vol. 2A.
[22] S. E. Miller, "Coupled wave theory and waveguide applications," *Bell System Technical Journal*, vol. 33, pp. 661 – 719, May 1954.
[23] C. L. Dolph, "A current distribution for broadside arrays which optimizes the relationship between beam width and side-lobe level," *Proceedings of the IRE*, vol. 34, no. 6, pp. 335–348, 1946.
[24] T. Taylor, "Design of line-source antennas for narrow beamwidth and low side lobes," *Antennas and Propagation, Transactions of the IRE Professional Group on*, vol. 3, no. 1, pp. 16–28, 1955.
[25] A. Villeneuve, "Taylor patterns for discrete arrays," *Antennas and Propagation, IEEE Transactions on*, vol. 32, no. 10, pp. 1089–1093, 1984.
[26] M. Ando, Y. Tsunemitsu, M. Zhang, J. Hirokawa, and S. Fujii, "Reduction of long line effects in single-layer slotted waveguide arrays with an embedded partially corporate feed," *Antennas and Propagation, IEEE Transactions on*, vol. 58, no. 7, pp. 2275–2280, 2010.

Lukui Jin (SM'12) received both his B.S. and M.S. degree in microwave engineering from Harbin Institute of Technology, Harbin, China, in 2008 and 2010, respectively. He is currently working toward the Ph.D. degree in the University of Leeds, Leeds, United Kingdom.

He is one of the 9 award holders of Leeds Fully-funded International Research Scholarship in 2010. His current research interests include design and analysis of substrate integrated waveguide, dielectric waveguide, and their applications in antennas and filters in the MCM technology.

Razak Mohd Ali Lee (SM'10) received both his B.Eng. and M.Eng. from Nagaoka University of Technology, Niigata, Japan, in 1999 and 2001, respectively. In 2001, he joined Tokyo Electron Limited, Tokyo, Japan, where he was a Field Engineer, then at the same year moved to Plasma Etching System Development and Manufacturing Centre at Tokyo Electron Yamanashi, Yamanashi, Japan. In 2006, he joined the School of Engineering and Information Technology, University Malaysia Sabah as a Lecturer. He is currently working towards the Ph.D degree in the University of Leeds, Leeds, United Kingdom.

His research interests involve multilayered-microwave device fabrication and its miniaturization techniques on LTCC and thick-film technology and integrated waveguides.

Ian Robertson (M'96- SM' 05 -Fellow 12) was born in London in 1963. He received his BSc (Eng) and PhD degrees from King's College London in 1984 and 1990, respectively. From 1984 to 1986 he worked in the MMIC Research Group at Plessey Research (Caswell). After that he returned to King's College London, initially as a Research Assistant and then as a Lecturer, finally becoming Reader in 1994. In 1998 he was appointed Professor of Microwave Subsystems Engineering at the University of Surrey, where he established the Microwave Systems Research Group and was a founder member of the Advanced Technology Institute.

He has organized many colloquia, workshops, and short courses for both the IEE and IEEE. He was the Honorary Editor of IEE Proceedings - Microwaves, Antennas & Propagation for many years and Editor-in-Chief of the rebranded IET Microwaves, Antennas & Propagation from 2005 to 2009. He edited the book 'MMIC Design' published by the IEE in 1995 and co-edited the book RFIC & MMIC Design and Technology, published in English 2001 and in Chinese in 2007. He has published over 400 papers in the areas of MIC and MMIC design. In June 2004 he was appointed to the University of Leeds Centenary Chair in Microwave and Millimeter-Wave Circuits and he is now Head of the School of Electronic & Electrical Engineering.